Unified-Actuator Nonlinear Dynamic Inversion Controller for the Variable Skew Quad Plane

De Ponti, Tomaso Maria Luigi; Smeur, Ewoud Jan Jacob; Remes, Bart Diane Walter

DOI
10.2514/1.G008659

Publication date
2025

Document Version
Final published version

Published in
Journal of Guidance, Control, and Dynamics

Citation (APA)
De Ponti, T. M. L., Smeur, E. J. J., & Remes, B. D. W. (2025). Unified-Actuator Nonlinear Dynamic Inversion Controller for the Variable Skew Quad Plane. *Journal of Guidance, Control, and Dynamics*, *48*(5), 1167-1176. https://doi.org/10.2514/1.G008659

JOURNAL OF GUIDANCE, CONTROL, AND DYNAMICS
Vol. 48, No. 5, May 2025

Technical Notes

Unified-Actuator Nonlinear Dynamic Inversion Controller for the Variable Skew Quad Plane

Tomaso Maria Luigi De Ponti,* Ewoud Jan Jacob Smeur,† and Bart Diane Walter Remes‡
Delft University of Technology, 2629 HS Delft, The Netherlands

https://doi.org/10.2514/1.G008659

Nomenclature

$C(u)$	=	cost function of WLS routine, -
c_x	=	cosine of angle x, -
$\boldsymbol{F_u}$	=	effectiveness matrix of the actuators, -
$\boldsymbol{F_x}$	=	effectiveness matrix of the state, -
G	=	effectiveness matrix of a general control law, -
$\boldsymbol{I}_{m\times m}$	=	identity matrix of size m, kg · m^2
I_{xx}	=	moment of Inertia of the drone around an axis x, kg · m^2
k_{x_y}	=	gain number x of block y, -
l_u	=	moment arm around center of gravity of actuator u, m
m	=	mass of the drone, kg
$\boldsymbol{P}$	=	position vector, m
$\boldsymbol{P}_{\text{des}}$	=	desired position vector, m
$\boldsymbol{P}_{\text{ref}}$	=	reference position vector, m
p_x	=	magnitude of location of pole x, -
s_x	=	sine of angle x, -
T_P	=	thrust of the pusher motors, N
T_Q	=	thrust of the quad-motors, N
u	=	state of actuator u, -
u_c	=	commanded state of actuator u, -
u_p	=	preferred state of actuator u in the WLS routine, -
$\boldsymbol{u_r}$	=	vector of real actuator state, -
$\boldsymbol{W_u}$	=	diagonal matrix of weighting factors of the actuators, -
$\boldsymbol{W_\nu}$	=	diagonal matrix of weighting factors of the pseudovector, -
$\boldsymbol{x}$	=	state vector, -
$\boldsymbol{y}$	=	output vector of a general system, -
γ	=	WLS primary objective weighting factor, -
ε_u	=	first-order dynamics corner frequency of actuator u, rad/s
$\boldsymbol{\eta}$	=	vector of attitude angles, rad
κ_{r_u}	=	torque curve linear coefficient of motor u, (N · m · s^2)/rad^2
κ_{T_u}	=	thrust curve linear coefficient of motor u, (N · s^2)/rad^2
Λ	=	skew angle, rad
$\boldsymbol{\nu}$	=	pseudocontrol vector, -
τ_x	=	first-order-dynamics time constant of actuator x, -
$\boldsymbol{\Omega}$	=	vector of angular rates, rad/s
ω_u	=	rotational speed of motor u, rad/s

Received 24 July 2024; accepted for publication 16 December 2024; published online Open Access 13 February 2025.

*Ph.D., Faculty of Aerospace Engineering, Control & Simulation; t.m.l.deponti@tudelft.nl (Corresponding Author).
†Assistant Professor, Faculty of Aerospace Engineering, Control & Simulation; e.j.j.smeur@tudelft.nl.
‡Project Manager, Faculty of Aerospace Engineering, Control & Simulation; b.d.w.remes@tudelft.nl.

I. Introduction

HYBRID unmanned aerial vehicles (UAVs) integrate both multicopter vertical takeoff and landing (VTOL) capabilities and the efficiency of winged flight, facilitated by a transition process. This combination of capabilities has opened up a myriad of applications, from urban package delivery to offshore missions. However, these applications often entail operating in challenging environments with strong and gusty winds. Thus, there is a pressing demand for UAV platforms capable of withstanding turbulent conditions and conducting autonomous operations.

The variable skew quad plane (VSQP) is a novel platform developed by TuDelft (Patent NL 2031701) specially designed to execute precise landings in windy conditions and on moving platforms. In [1,2], the control of the VSQP was accomplished using incremental nonlinear dynamic inversion (INDI) with weighted least squares (WLS) [3,4] control allocation. One of the main benefits of INDI over, for example, proportional integral and derivative control in the realm of micro air vehicles (MAVs) is its demonstrated capability for rapid disturbance rejection [5,6]. This capability has also been verified for winged platforms [7]. It is evident how disturbance rejection is a critical requirement for a platform intended for precise landings in windy conditions or on moving platforms.

As shown in [8], another advantage is the minimal requirement for modeling knowledge and gain tuning to develop an INDI controller. Ref. [1] provides a comprehensive overview of control for the VSQP, demonstrating how a few simple assumptions and models enable accurate control effectiveness estimation and control. Likewise, [2] reaches similar conclusions but with an emphasis on guidance.

Whereas [1] and [2] only make use of simple error controllers (ECs) to track desired pseudocontrol vectors, Refs. [9] and [10] show that reference models can be used to generate feasible smooth reference trajectories directly from the control variables. This allows for better definition of the response dynamics of the platform as well as detection of deviations from desired trajectories at all derivative levels.

As for the structure of the controller, [1,5,7] propose a cascaded implementation in which two nested control allocation routines try to satisfy attitude and position demands. Instead, [9–11] develop a unified controller structure that makes use of a single dynamic inversion procedure to track a given pseudocontrol vector. This method, when combined with a WLS approach, offers the advantage of enabling the definition of a hierarchy in control allocation between position and attitude requirements, particularly in situations where the actuators effective in both domains become saturated. The method has been proven to robustly provide control for transitioning hybrid VTOL aircraft with actuators capable of generating both forces and moments.

In INDI, the control law lacks a representation of actuator dynamics and entirely neglects state-induced effects. It is assumed, as in the work of [12], that the state- dependent term changes sufficiently slow compared to the actuator dynamics. However, a real-life actuator, which often can be modeled as a first- or second-order system, would suffer from lag as well as attenuation of amplitude.

In [13], the state change is incorporated over one time step. However, this approach is limited when actuator dynamics are significant, as the anticipated state change is not realized within one time sample. In [14], the state-dependent terms are added in discrete time, but this method also struggles with actuator time constants larger than

the controller's time step, leading to potential large actuator inputs and hidden oscillations.

In [15], pseudocontrol hedging is proposed to prevent a controller from adapting to system input characteristics such as actuator dynamics. In [9], the hedging effect is incorporated by recalculating the highest-order derivative and moving the reference model in the opposite direction (hedge) by an estimate of the amount that the plant did not move due to actuator dynamics.

In an effort to develop a more comprehensive compensation technique for actuator dynamics and state-dependent terms, [16–18] integrate knowledge of the actuators' dynamics directly into the control allocation process. This involves formulating an INDI control law based on an additional time derivative of the system output, thereby incorporating information about the actuators' response dynamics directly into the effectiveness matrix. This control law is termed actuator nonlinear dynamic inversion (ANDI) by [18].

In the control of the VSQP, precise trajectory tracking during transition and landing has proven to be challenging. These difficulties primarily stem from the slow attitude dynamics, leading to erroneous control allocation with other fast actuators like the pusher motor. The contributions of this Technical Note are the following: 1) the first implementation and flight testing of the ANDI control law on a real platform, 2) the first proposal of a method to extend the ANDI control law for guidance operations and its application to higher-order dynamic actuators, 3) the first integration of the ANDI control law within a unified controller structure, and 4) an in-depth comparative analysis of the real-world performance of INDI and ANDI controllers in trajectory and desired state tracking.

II. The Variable Skew Quad Plane

In hovering, the drone functions as a quad-rotor, with attitude control achieved through differential thrust. During forward flight, the drone behaves like a plane, utilizing aerodynamic surfaces for attitude control. Similar to a typical quad-plane configuration, the drone gains forward speed from a push propeller located at the tail. However, unlike a traditional quad-plane design, in the proposed configuration the wing is not fixed. Instead, it employs the rotating concept akin to that used in an oblique flying wing [19]. A central rotating structure facilitates wing deployment while the lateral rotors are folded into the fuselage. This approach is anticipated to significantly enhance cruise efficiency by leveraging the lift generation benefits of the wings and reducing drag through the retraction of unused rotors. Furthermore, in hover mode, positioning the wing atop the fuselage reduces the area susceptible to wind gusts, consequently enhancing control authority. Figures 1 and 2 depict the VSQP in hover and forward flight modes, respectively. The VSQP employs a total of 10 actuators, detailed in Table 1. Additionally, a graphical depiction of the actuators' placement on the VSQP is presented in Fig. 3. The right-hand column of the table indicates whether each actuator rotates with the skew angle.

The control of the VSQP is intricate, due to several factors. The coupling of certain actuators with the skew angle introduces variability in their effectiveness. Additionally, the lift generated by the wing is a function of both the skew angle and airspeed, adding further complexity. Moreover, the broad flight envelope is achieved through a transition between hovering, where the quad motors are primarily utilized for control, and forward flight, where the aerodynamic surfaces come into play.

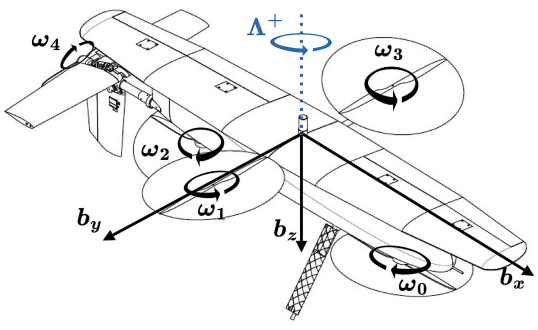

Fig. 1 VSQP with skew angle Λ set to 0 deg.

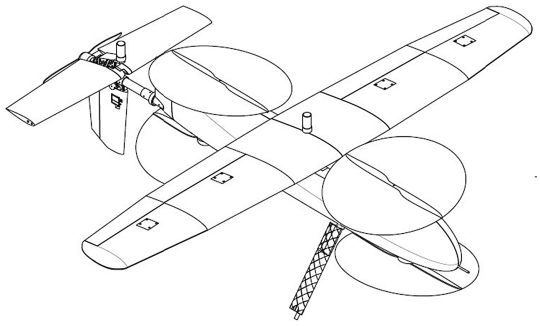

Fig. 2 VSQP with skew angle Λ set to 90 deg.

Table 1 List of actuators for the VSQP

No.	Actuator	Symbol	Rotates
1	Front motor	m_0	— —
2	Right motor	m_1	✓
3	Back motor	m_2	— —
4	Left motor	m_3	✓
5	Pusher motor	m_4	— —
6	Elevator	e	— —
7	Rudder	r	— —
8	Ailerons	a	✓
9	Flaps	f	✓
10	Rotation servo	R_Λ	— —

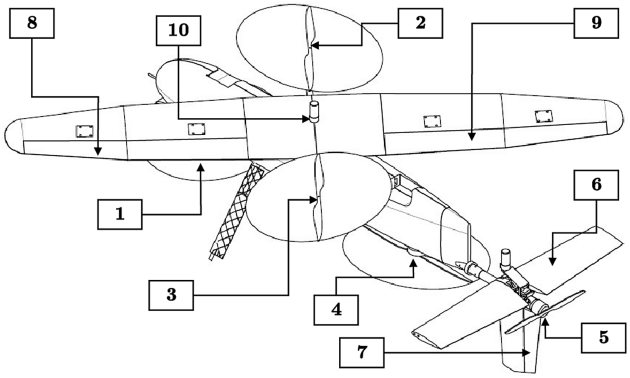

Fig. 3 Actuator schematic of the VSQP.

III. Unified Control Approach

One approach to organizing an INDI controller is to employ a cascaded structure. In this setup, an outer loop guidance controller provides inputs to an inner loop attitude controller. An example of such a cascaded control structure for a quadcopter is illustrated in Fig. 4. The control allocation blocks vary in structure depending on the specific control law employed. Lastly, the MAV block represents the dynamics of the drone.

In Fig. 4, it is evident that the command signal to the actuators results from two cascaded optimization routines. When an actuator is highly effective in both generating a moment around the center of gravity for attitude control and producing a force for guidance, it becomes less straightforward how the final actuator command is computed. In contrast, the unified controller computes a single control allocation to simultaneously address linear and angular acceleration goals. This consolidation integrates guidance and stabilization into a unified control allocation for two sets of actuators. The first set

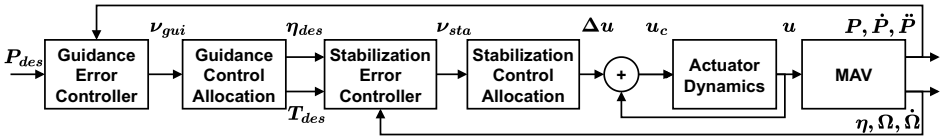

Fig. 4 Conventional cascaded control structure substituted by the unified controller.

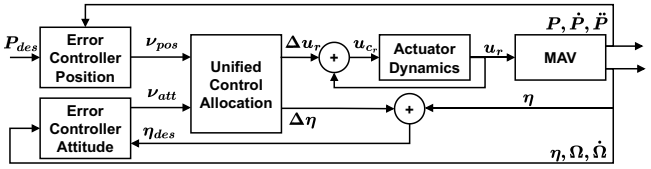

Fig. 5 Example of unified control structure.

comprises the real actuators, such as motors and servos. The second set consists of virtual actuators, which, in the simplified control scenario depicted in Fig. 5, are represented by the attitude angles.

Thanks to the unified structure and single control allocation, complemented by a WLS routine, implementing actuator cost functions becomes more straightforward. The cost function for the WLS routine, as outlined in [1,3], is expressed as

$$C(u) = \underbrace{\|W_u(u-u_p)\|^2}_{\text{Secondary Objective}} + \gamma \underbrace{\|W_v(Gu-\nu)\|^2}_{\text{Primary Objective}} = \left\| \begin{bmatrix} \gamma^{\frac{1}{2}} W_v G \\ W_u \end{bmatrix} u - \begin{bmatrix} \gamma^{\frac{1}{2}} W_v \nu \\ W_u u_p \end{bmatrix} \right\|^2 \tag{1}$$

This cost function can be minimized by solving the associated quadratic programming problem to determine the actuator state vector that reduces the cost while adhering to the actuators' saturation limits. By assigning different weights in W_v, the designer can establish a hierarchy in control allocation, prioritizing position or attitude requirements according to their preferences. Such a hierarchy is particularly valuable when actuators effective in both domains reach saturation. For instance, during a transition phase, the VSQP can increase altitude by either increasing the quad thrust or adjusting the pitch angle to generate more lift. When the quad motors are commanded to reach saturation, the control allocation mechanism needs to determine whether to prioritize achieving a new attitude or generating more linear acceleration. The unified structure has been demonstrated to robustly provide control for transitioning hybrid VTOL aircraft equipped with actuators capable of producing both forces and moments [11].

IV. Actuator Nonlinear Dynamic Inversion

In INDI, control allocation challenges arise when attempting to distribute the control action to multiple actuators with significantly different dynamics, such as in the case of the attitude and real actuators within the unified control approach. This occurs because the effectiveness matrix provides information solely on the effectiveness of an actuator, without considering its dynamics. As a consequence, two actuators with equal effectiveness along a controlled axis x, and equal weighting in the control allocation, but differing dynamics and effectiveness along other axes, will receive equivalent commands to achieve the desired pseudocontrol vector along that axis, $\boldsymbol{\nu}_x$. However, although the faster actuator may promptly reach its commanded value, the slower one will lag behind, leading to an imbalance and imperfect tracking across all axes.

In their work, Steffensen et al. [18] introduce ANDI, a novel extension of the nonlinear dynamic inversion control law for systems characterized by varying and nonnegligible first-order actuator dynamics, defined as

$$\dot{\boldsymbol{u}} = \boldsymbol{\varepsilon}_{\boldsymbol{u}}(\boldsymbol{u}_{\boldsymbol{c}} - \boldsymbol{u}) = \boldsymbol{\varepsilon}_{\boldsymbol{u}}\Delta\boldsymbol{u} \tag{2}$$

where

$$\boldsymbol{\varepsilon}_{\boldsymbol{u}} = \text{diag}(\varepsilon_{m_0}, \varepsilon_{m_1}, \varepsilon_{m_2}, \varepsilon_{m_3}, \varepsilon_{m_4}, \varepsilon_e, \varepsilon_r, \varepsilon_a, \varepsilon_f, \varepsilon_\phi, \varepsilon_\theta) \tag{3}$$

The derivation of the ANDI control law starts from the definition of a general system for the VSQP:

$$\begin{aligned} \dot{\tilde{\boldsymbol{x}}} &= \tilde{\boldsymbol{f}}(\tilde{\boldsymbol{x}}, \boldsymbol{u}_r), \\ \boldsymbol{y} &= \boldsymbol{h}(\tilde{\boldsymbol{x}}, \boldsymbol{u}_r) \end{aligned} \tag{4}$$

where

$$\begin{aligned} \tilde{\boldsymbol{x}} &= [\boldsymbol{x}, \boldsymbol{u}_v]^T, \\ \boldsymbol{x} &= \left[\dot{P}_N, \dot{P}_E, \dot{P}_D, \Omega_x, \Omega_y, \Omega_z\right]^T, \\ \boldsymbol{u}_v &= [\phi, \theta]^T, \\ \boldsymbol{u}_r &= \left[\omega_{m_0}^2, \omega_{m_1}^2, \omega_{m_2}^2, \omega_{m_3}^2, \omega_{m_4}^2\right]^T \end{aligned} \tag{5}$$

Similar to [10], we distinguish between nondirectly controlled states $\boldsymbol{x}$ and the states used as virtual actuators $\boldsymbol{u}_v$. The system's output is expressed as a subset of the time derivative of the total state vector corresponding to the non-directly controlled states:

$$\boldsymbol{y} = \boldsymbol{h}(\tilde{\boldsymbol{x}}, \boldsymbol{u}_r) = \dot{\boldsymbol{x}} = \boldsymbol{f}(\boldsymbol{x}, \boldsymbol{u}) = \left[\ddot{P}_N, \ddot{P}_E, \ddot{P}_D, \dot{\Omega}_x, \dot{\Omega}_y, \dot{\Omega}_z\right]^T \tag{6}$$

where the general actuator state vector $\boldsymbol{u}$ is defined as $[\boldsymbol{u}_r, \boldsymbol{u}_v]$. Performing a differentiation in time and using the actuator dynamics definition of Eq. (2) leads to

$$\dot{\boldsymbol{y}} = \frac{\partial \boldsymbol{f}(\boldsymbol{x}, \boldsymbol{u})}{\partial \boldsymbol{x}}\dot{\boldsymbol{x}} + \frac{\partial \boldsymbol{f}(\boldsymbol{x}, \boldsymbol{u})}{\partial \boldsymbol{u}}\dot{\boldsymbol{u}} = \boldsymbol{F}_{\boldsymbol{x}}\dot{\boldsymbol{x}} + \boldsymbol{F}_{\boldsymbol{u}}\dot{\boldsymbol{u}} = \boldsymbol{F}_{\boldsymbol{x}}\dot{\boldsymbol{x}} + \boldsymbol{F}_{\boldsymbol{u}}\boldsymbol{\varepsilon}_{\boldsymbol{u}}\Delta\boldsymbol{u} \tag{7}$$

Now, by setting the pseudocontrol vector $\boldsymbol{\nu}$ equal to $\dot{\boldsymbol{y}}$, assuming $\boldsymbol{F}_{\boldsymbol{u}}\boldsymbol{\varepsilon}_{\boldsymbol{u}}$ is full rank and taking its pseudoinverse, and rearranging Eq. (7), we derive the ANDI control law:

$$\Delta\boldsymbol{u} = (\boldsymbol{F}_{\boldsymbol{u}}\boldsymbol{\varepsilon}_{\boldsymbol{u}})^{+}(\boldsymbol{\nu} - \boldsymbol{F}_{\boldsymbol{x}}\dot{\boldsymbol{x}}) \tag{8}$$

In Eq. (8), the effectiveness matrix $\boldsymbol{F}_{\boldsymbol{u}}$ consists of subcomponents associated with the quad motors (Q), the pusher motor (P), and the attitude angles (η). As outlined in [1] and [2], it is defined as

$$\boldsymbol{F}_{\boldsymbol{u}} = \text{diag}(m, m, m, I_{xx}, I_{yy}, I_{zz})^{-1}\left[\boldsymbol{F}_{\boldsymbol{u}_Q}, \boldsymbol{F}_{\boldsymbol{u}_P}, \boldsymbol{F}_{\boldsymbol{u}_\eta}\right] \tag{9}$$

$$\boldsymbol{F}_{\boldsymbol{u}_Q} = \begin{bmatrix} (c_\psi s_\theta + c_\theta s_\phi s_\psi)\kappa_{T_{m_1}} & (c_\psi s_\theta + c_\theta s_\phi s_\psi)\kappa_{T_{m_0}} & (c_\psi s_\theta + c_\theta s_\phi s_\psi)\kappa_{T_{m_2}} & (c_\psi s_\theta + c_\theta s_\phi s_\psi)\kappa_{T_{m_3}} \\ (s_\psi s_\theta - c_\psi c_\theta s_\phi)\kappa_{T_{m_0}} & (s_\psi s_\theta - c_\psi c_\theta s_\phi)\kappa_{T_{m_1}} & (s_\psi s_\theta - c_\psi c_\theta s_\phi)\kappa_{T_{m_2}} & (s_\psi s_\theta - c_\psi c_\theta s_\phi)\kappa_{T_{m_3}} \\ (c_\phi c_\theta)\kappa_{T_{m_0}} & (c_\phi c_\theta)\kappa_{T_{m_1}} & (c_\phi c_\theta)\kappa_{T_{m_2}} & (c_\phi c_\theta)\kappa_{T_{m_3}} \\ 0 & -c_\Lambda l_{m_1}\kappa_{T_{m_1}} & 0 & c_\Lambda l_{m_3}\kappa_{T_{m_3}} \\ l_{m_0}\kappa_{T_{m_0}} & s_\Lambda l_{m_1}\kappa_{T_{m_1}} & -l_{m_2}\kappa_{T_{m_2}} & -s_\Lambda l_{m_3}\kappa_{T_{m_3}} \\ -\kappa_{r_{m_0}} & \kappa_{r_{m_1}} & -\kappa_{r_{m_2}} & \kappa_{r_{m_3}} \end{bmatrix} \tag{10}$$

$$\boldsymbol{F}_{\boldsymbol{u}_P} = \begin{bmatrix} (c_\psi c_\theta - s_\phi s_\psi s_\theta)\kappa_{T_{m_4}} \\ (c_\theta s_\psi + c_\psi s_\phi s_\theta)\kappa_{T_{m_4}} \\ (-c_\phi s_\theta)\kappa_{T_{m_4}} \\ 0 \\ 0 \\ 0 \end{bmatrix} \tag{11}$$

$$\boldsymbol{F}_{\boldsymbol{u}_\eta} = \begin{bmatrix} c_\phi c_\theta s_\psi T_Q - c_\phi s_\psi s_\theta T_P & (c_\theta c_\psi - s_\phi s_\theta s_\psi)T_Q - (c_\psi s_\theta + c_\theta s_\phi s_\psi)T_P \\ -c_\phi c_\theta c_\psi T_Q + c_\phi c_\psi s_\theta T_P & (c_\theta s_\psi + s_\phi s_\theta c_\psi)T_Q - (s_\psi s_\theta - c_\psi c_\theta s_\phi)T_P \\ -s_\phi c_\theta T_Q + s_\phi s_\theta T_P & -s_\theta c_\phi T_Q - c_\phi c_\theta T_P \\ 0 & 0 \\ 0 & 0 \\ 0 & 0 \end{bmatrix} \tag{12}$$

where

$$T_Q = \frac{\kappa_{T_{m_0}}\omega_0^2 + \kappa_{T_{m_1}}\omega_1^2 + \kappa_{T_{m_2}}\omega_2^2 + \kappa_{T_{m_3}}\omega_3^2}{4} \tag{13}$$

$$T_P = \kappa_{T_{m_4}}\omega_4^2 \tag{14}$$

It is important to note that, unlike in [1,2], no effectiveness values for the aerodynamic surfaces and lift are provided in this study. This omission is due to the fact that the tests presented here are conducted indoors and at a negligible airspeed. Therefore, for clarity, these effectiveness values are omitted.

From Eq. (8), it is evident that in ANDI, aside from directly incorporating knowledge of actuator dynamics in the matrix inversion, one can also compensate the state-induced effects $\boldsymbol{F}_{\boldsymbol{x}}$ if known. However, for the purposes of this study, which includes validation tests conducted indoors where the velocities and angular rates ($\dot{\boldsymbol{x}}$) are small, we will assume these effects to be negligible. This simplifies the command law to the form given by Eq. (15).

$$\Delta\boldsymbol{u} = (\boldsymbol{F}_{\boldsymbol{u}}\boldsymbol{\varepsilon}_{\boldsymbol{u}})^+(\boldsymbol{\nu}) \tag{15}$$

We observe that in an effort to track $\boldsymbol{\nu}$, actuators with faster dynamics $\boldsymbol{\varepsilon}_{\boldsymbol{u}}$ will receive smaller commands compared to actuators with slower dynamics. This effectively embeds knowledge of the actuators' dynamics directly into the effectiveness matrix.

V. Incremental Nonlinear Dynamic Inversion

In [18], the INDI control law is derived from the ANDI control law under the assumption of ideal actuators with infinite ε. This derivation is particularly noteworthy, as it also introduces a method for designing consistent ECs tailored to the two control laws. Notably, [18] proposes a structured approach to the general error dynamics of the system, modeling it as a cascade of two components: a slower system representing the desired error dynamics and a faster inner loop with a corner frequency ε_y, designed to capture the faster actuator dynamics. Using the notation of this Note, the error dynamics in the Laplace domain can be expressed as

$$\boldsymbol{E}_{\boldsymbol{y}}(s)\left(s^2\boldsymbol{I} + \sum_{i=0}^{1} s^i \boldsymbol{k}_{i+1_{\text{ec}}}\right)(s\boldsymbol{I} + \boldsymbol{\varepsilon}_{\boldsymbol{y}}) = 0 \tag{16}$$

where $\boldsymbol{e}_{\boldsymbol{y}} = \boldsymbol{y}_{\text{ref}} - \boldsymbol{y}$ is the error in $\boldsymbol{y}$ with Laplace transform $\boldsymbol{E}_{\boldsymbol{y}}(s)$, $(s^2\boldsymbol{I} + \sum_{i=0}^{1} s^i \boldsymbol{k}_{i+1_{\text{ec}}})$ describes the desired error dynamics with respect to the system, $(s\boldsymbol{I} + \boldsymbol{\varepsilon}_{\boldsymbol{y}})$ is the desired error dynamics due to the first-order actuators, and $\boldsymbol{k}$ are the gains of the parallel EC. Expanding Eq. (16), transforming to the time domain and setting the pseudocontrol vector $\boldsymbol{\nu}$ to $\ddot{\boldsymbol{y}}$ leads to

$$\boldsymbol{\nu} = \ddot{\boldsymbol{y}}_{\text{ref}} + (\boldsymbol{k}_{2_{\text{ec}}} + \boldsymbol{\varepsilon}_{\boldsymbol{y}})\ddot{\boldsymbol{e}}_y + (\boldsymbol{\varepsilon}_{\boldsymbol{y}}\boldsymbol{k}_{2_{\text{ec}}} + \boldsymbol{k}_{1_{\text{ec}}})\dot{\boldsymbol{e}}_y + \boldsymbol{\varepsilon}_{\boldsymbol{y}}\boldsymbol{k}_{1_{\text{ec}}}\boldsymbol{e}_y \tag{17}$$

It is also possible to redefine Eq. (17) so that $\boldsymbol{k}$ represents the gains of a cascaded EC, similar to the one proposed later in Sec. VI for INDI:

$$\boldsymbol{\nu} = \ddot{\boldsymbol{y}}_{\text{ref}} + (\boldsymbol{k}_{2_{\text{ec}}} + \boldsymbol{\varepsilon}_{\boldsymbol{y}})\ddot{\boldsymbol{e}}_y + (\boldsymbol{\varepsilon}_{\boldsymbol{y}}\boldsymbol{k}_{2_{\text{ec}}} + \boldsymbol{k}_{1_{\text{ec}}}\boldsymbol{k}_{2_{\text{ec}}})\dot{\boldsymbol{e}}_y + \boldsymbol{\varepsilon}_{\boldsymbol{y}}\boldsymbol{k}_{1_{\text{ec}}}\boldsymbol{k}_{2_{\text{ec}}}\boldsymbol{e}_y \tag{18}$$

The control law of ANDI reported in Eq. (8) can then be reformulated to

$$\begin{aligned} \Delta\boldsymbol{u} &= (\boldsymbol{F}_{\boldsymbol{u}}\boldsymbol{\varepsilon}_{\boldsymbol{u}})^+\big(\ddot{\boldsymbol{y}}_{\text{ref}} + (\boldsymbol{k}_{2_{\text{ec}}} + \boldsymbol{\varepsilon}_{\boldsymbol{y}})\ddot{\boldsymbol{e}}_y + (\boldsymbol{\varepsilon}_{\boldsymbol{y}}\boldsymbol{k}_{2_{\text{ec}}} + \boldsymbol{k}_{1_{\text{ec}}}\boldsymbol{k}_{2_{\text{ec}}})\dot{\boldsymbol{e}}_y \\ &\quad + \boldsymbol{\varepsilon}_{\boldsymbol{y}}\boldsymbol{k}_{1_{\text{ec}}}\boldsymbol{k}_{2_{\text{ec}}}\boldsymbol{e}_y - \boldsymbol{F}_{\boldsymbol{x}}\dot{\boldsymbol{x}}\big) \\ &= (\boldsymbol{F}_{\boldsymbol{u}}\boldsymbol{\varepsilon}_{\boldsymbol{u}})^+\big(\ddot{\boldsymbol{y}}_{\text{ref}} + \boldsymbol{k}_{2_{\text{ec}}}\ddot{\boldsymbol{e}}_y + \boldsymbol{k}_{1_{\text{ec}}}\boldsymbol{k}_{2_{\text{ec}}}\dot{\boldsymbol{e}}_y - \boldsymbol{F}_{\boldsymbol{x}}\dot{\boldsymbol{x}} \\ &\quad + \boldsymbol{\varepsilon}_{\boldsymbol{y}}(\ddot{\boldsymbol{e}}_y + \boldsymbol{k}_{2_{\text{ec}}}\dot{\boldsymbol{e}}_y + \boldsymbol{k}_{1_{\text{ec}}}\boldsymbol{k}_{2_{\text{ec}}}\boldsymbol{e}_y)\big) \end{aligned} \tag{19}$$

Now, assuming that all actuators have the same dynamics, such that $\boldsymbol{\varepsilon}_u = \varepsilon_u \boldsymbol{I}_{\|u\|\times\|u\|}$, and choosing accordingly $\boldsymbol{\varepsilon}_{\boldsymbol{y}} = \varepsilon_u \boldsymbol{I}_{\|y\|\times\|y\|}$, it is possible to derive that

$$\begin{aligned} \Delta\boldsymbol{u} &= \frac{1}{\varepsilon_u}(\boldsymbol{F}_{\boldsymbol{u}})^+\big(\ddot{\boldsymbol{y}}_{\text{ref}} + \boldsymbol{k}_{2_{\text{ec}}}\ddot{\boldsymbol{e}}_y + \boldsymbol{k}_{1_{\text{ec}}}\boldsymbol{k}_{2_{\text{ec}}}\dot{\boldsymbol{e}}_y - \boldsymbol{F}_{\boldsymbol{x}}\dot{\boldsymbol{x}}\big) \\ &\quad + (\boldsymbol{F}_{\boldsymbol{u}})^+\big(\ddot{\boldsymbol{e}}_y + \boldsymbol{k}_{2_{\text{ec}}}\dot{\boldsymbol{e}}_y + \boldsymbol{k}_{1_{\text{ec}}}\boldsymbol{k}_{2_{\text{ec}}}\boldsymbol{e}_y\big) \end{aligned} \tag{20}$$

Letting the actuator dynamics ε approach infinity leads to

$$\begin{aligned} \Delta\boldsymbol{u} &= \lim_{\varepsilon_u\to\infty}\left(\frac{1}{\varepsilon_u}(\boldsymbol{F}_{\boldsymbol{u}})^+\big(\ddot{\boldsymbol{y}}_{\text{ref}} + \boldsymbol{k}_{2_{\text{ec}}}\ddot{\boldsymbol{e}}_y + \boldsymbol{k}_{1_{\text{ec}}}\boldsymbol{k}_{2_{\text{ec}}}\dot{\boldsymbol{e}}_y - \boldsymbol{F}_{\boldsymbol{x}}\dot{\boldsymbol{x}}\big)\right. \\ &\quad \left. + (\boldsymbol{F}_{\boldsymbol{u}})^+\big(\ddot{\boldsymbol{e}}_y + \boldsymbol{k}_{2_{\text{ec}}}\dot{\boldsymbol{e}}_y + \boldsymbol{k}_{1_{\text{ec}}}\boldsymbol{k}_{2_{\text{ec}}}\boldsymbol{e}_y\big)\right) \\ &= (\boldsymbol{F}_{\boldsymbol{u}})^+\big(\ddot{\boldsymbol{e}}_y + \boldsymbol{k}_{2_{\text{ec}}}\dot{\boldsymbol{e}}_y + \boldsymbol{k}_{1_{\text{ec}}}\boldsymbol{k}_{2_{\text{ec}}}\boldsymbol{e}_y\big) \\ &= (\boldsymbol{F}_{\boldsymbol{u}})^+\big(\ddot{\boldsymbol{y}}_{\text{ref}} + \boldsymbol{k}_{2_{\text{ec}}}\dot{\boldsymbol{e}}_y + \boldsymbol{k}_{1_{\text{ec}}}\boldsymbol{k}_{2_{\text{ec}}}\boldsymbol{e}_y - \ddot{\boldsymbol{y}}\big) \\ &= (\boldsymbol{F}_{\boldsymbol{u}})^+(\boldsymbol{\upsilon} - \ddot{\boldsymbol{y}}) \end{aligned} \tag{21}$$

where $\boldsymbol{\upsilon}$ is the pseudocontrol vector calculated by a second-order cascaded EC. Equation (21) is nothing other than the INDI control law as reported in literature [1]. Therefore, it can be concluded that under the assumption of infinitely fast actuators, the INDI control law approximates the exact ANDI control law. In addition, with the proposed error dynamics structure, it is possible to relate the gains of a second-order INDI EC to the gains of a third-order ANDI EC, given the actuator dynamics.

VI. Reference Model and Error-Controller-Poles-Based Design

In [1], control objectives are derived solely from linear ECs. These ECs, as shown in Fig. 4, process the desired positions and attitudes to

linearly calculate the required adjustments in linear and angular accelerations. This framework, however, does not facilitate the explicit definition of other higher-order reference signals that one might wish to track. For instance, during transition, commanding a specified position might not be the only goal; specifying a particular velocity and acceleration envelope could also be desired. These higher-order reference signals can be formulated and bounded where needed, using a reference model (RM). A sample RM is illustrated in Fig. 6.

An adapted version of the EC that accepts multiple reference signals as input is provided in Figs. 7 and 8 for ANDI and INDI, respectively. The RM in Fig. 6 can be captured with the following transfer function with negative real poles with magnitude p_1, p_2, and p_3:

$$H_{3\text{rd}}(s) = \frac{p_1}{s+p_1}\frac{p_2}{s+p_2}\frac{p_3}{s+p_3} = \frac{p_1p_2p_3}{s^3+(p_1+p_2+p_3)s^2+(p_1p_2+p_1p_3+p_2p_3)s+p_1p_2p_3} \tag{22}$$

The transfer function for the RM can be calculated by block-reducing the diagram in Fig. 6, leading to

$$H_{\text{rm}}(s) = \frac{k_{1_{\text{rm}}}k_{2_{\text{rm}}}k_{3_{\text{rm}}}}{s^3+k_{3_{\text{rm}}}s^2+k_{2_{\text{rm}}}k_{3_{\text{rm}}}s+k_{1_{\text{rm}}}k_{2_{\text{rm}}}k_{3_{\text{rm}}}} \tag{23}$$

The same transfer function can be derived for the EC dynamics of Fig. 7. In essence, the gains of RMs or ECs can be calculated as a function of the poles of a third-order system by comparing the coefficients of the denominators of Eqs. (22) and (23):

$$k_1 = \frac{p_1p_2p_3}{p_1p_2+p_1p_3+p_2p_3}, \quad k_2 = \frac{p_1p_2+p_1p_3+p_2p_3}{p_1+p_2+p_3}, \quad k_3 = p_1+p_2+p_3 \tag{24}$$

Consequently, it becomes possible to design pole positions to realize a specific desired dynamics and then translate those pole positions into gains for RM and EC. This methodology offers a significant benefit by enabling the explicit design of the system's response based on well-established Linear Time-Invariant (LTI) systems theory. It is important to note that in this Note we primarily focus on systems with real poles to achieve a critically damped response of the system. However, the same conclusions could be drawn for a system with a real pole and a pair of imaginary conjugate poles.

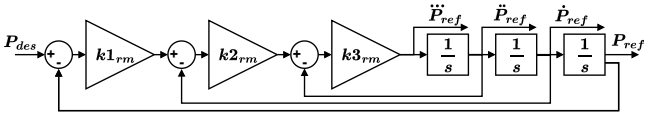

Fig. 6 Position reference model.

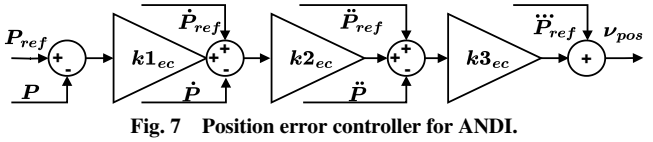

Fig. 7 Position error controller for ANDI.

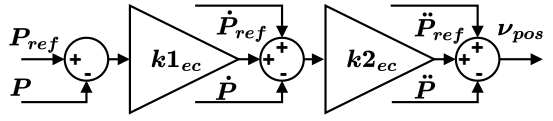

Fig. 8 Position error controller for INDI.

VII. ANDI and INDI Theoretical Comparison

Figure 9 presents a modified version of the unified controller depicted in Fig. 5. This version incorporates the ANDI control law through Moore–Penrose pseudoinversion of the effectiveness matrix, along with the RMs and ECs discussed earlier. Additionally, the desired attitude angles are no longer calculated using the output of the MAV block. Instead, they are explicitly determined using the attitude dynamics described in $\boldsymbol{\varepsilon_u}$. Both approaches yield equivalent results, provided the utilized attitude dynamics accurately reflect the real attitude dynamics and no external disturbances influence the attitude angles.

The last block to be analyzed is the MAV block, which in real-life applications is accompanied by an inertial navigation system and sensor readings. This block contains the transfer function $\dot{\boldsymbol{x}}(s)/\boldsymbol{u}(s)$ and integration blocks to output the state and its derivatives, which are then fed back to the ECs. For a linear system, assuming the state-dependent term is negligible, this transfer function is equivalent to $\boldsymbol{F_u}(\boldsymbol{x}_0, \boldsymbol{u}_0)$. Consequently, for a single input single output (SISO) system, one can see how the signal path from the pseudocontrol vector up to and including the MAV block can be reduced to just an integrator.

By further rearranging the block diagram of the ECs with the extra integrator for a single signal path, we discover that $\boldsymbol{P}(s)/\boldsymbol{P}_{\text{ref}}(s)$ and $\boldsymbol{\eta}(s)/\boldsymbol{\eta}_{\text{ref}}(s)$ reduce to unity gains. In other words, with ANDI, the transfer functions from $\boldsymbol{P}(s)/\boldsymbol{P}_{\text{des}}(s)$ and $\boldsymbol{\eta}(s)/\boldsymbol{\eta}_{\text{des}}(s)$ are simplified to $\boldsymbol{P}_{\text{ref}}(s)/\boldsymbol{P}_{\text{des}}(s)$ and $\boldsymbol{\eta}_{\text{ref}}(s)/\boldsymbol{\eta}_{\text{des}}(s)$, respectively.[§] The same cannot be said for an INDI unified controller with the ECs, as depicted in Fig. 8. In this case, the transfer functions $\boldsymbol{P}(s)/\boldsymbol{P}_{\text{ref}}(s)$ and $\boldsymbol{\eta}(s)/\boldsymbol{\eta}_{\text{ref}}(s)$ do not reduce to simple unity gains. Instead, they become dependent on the respective error-controller gains and actuator dynamics:

$$\frac{\boldsymbol{\eta}(s)}{\boldsymbol{\eta}_{\text{ref}}(s)_{\text{INDI}}} = \frac{\varepsilon_u(s^2+k_{2_{\text{ec}}}s+k_{1_{\text{ec}}}k_{2_{\text{ec}}})}{s^3+\varepsilon_u s^2+k_{2_{\text{ec}}}\varepsilon_u s+k_{1_{\text{ec}}}k_{2_{\text{ec}}}\varepsilon_u} \tag{25}$$

In a nutshell, under the assumption that actuator dynamics can be accurately represented by a first-order model, perfect inversion becomes feasible with ANDI. On one hand, this assumption is typically valid for nonsaturated real actuators allowing their corner frequency to be utilized in control allocation. On the other hand, this does not hold true for virtual actuators, such as attitude angles. In ANDI, as deduced earlier, the dynamics of the attitude angles $\boldsymbol{\eta}(s)/\boldsymbol{\eta}_{\text{des}}(s)$ correspond to the dynamics of the attitude reference model $\boldsymbol{\eta}_{\text{ref}}(s)/\boldsymbol{\eta}_{\text{des}}(s)$, which, in turn, is a third-order system. Hence, to incorporate virtual actuators into control allocation, we must approximate the attitude dynamics to a first-order system and evaluate the impact of this introduced inaccuracy. To this end, consider the Taylor expansion of an exponential function:

$$e^x \simeq 1 + x + \frac{x^2}{2} + \frac{x^3}{6} + \frac{x^4}{24} + \frac{x^5}{120} + O(x^6) \tag{26}$$

Now, truncating the approximation of Eq. (26) at the second term allows us to introduce the relation of Eq. (27). By adopting this approach, we are already aware that we are introducing inaccuracies in the high-frequency regime. A more thorough analysis of these inaccuracies will be conducted later. Using such a Taylor expansion, it is possible to derive a mathematical approximation of a first-order system with time constant τ:

$$e^{-\tau s} = \frac{1}{e^{\tau s}} \approx \frac{1}{1+\tau s} \tag{27}$$

Starting from the transfer function of a third-order system as depicted in Eq. (22):

[§]Find all block-reduction derivations at [20].

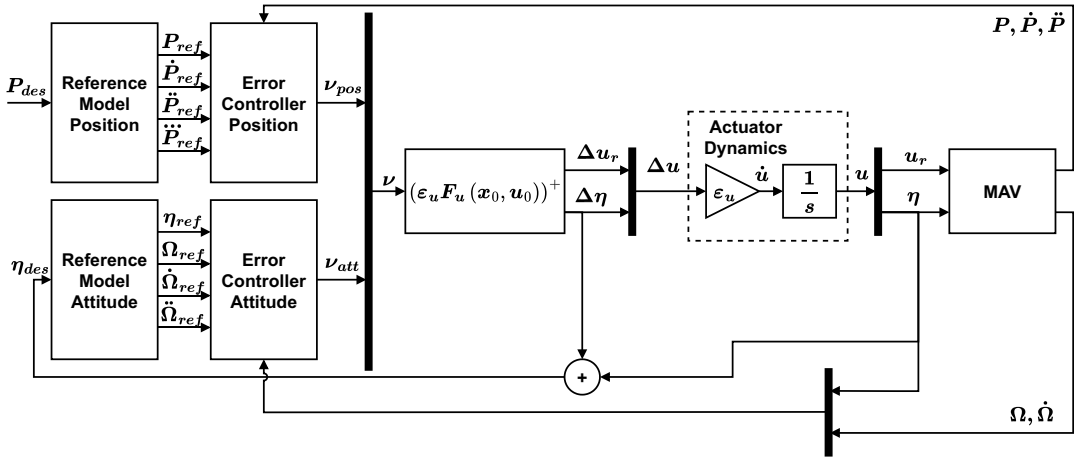

Fig. 9 Diagram of the unified ANDI controller.

$$H_{3\text{rd}}(s) = \frac{p_1}{s+p_1}\frac{p_2}{s+p_2}\frac{p_3}{s+p_3} = \frac{1}{\left(\frac{1}{p_1}s+1\right)\left(\frac{1}{p_2}s+1\right)\left(\frac{1}{p_3}s+1\right)} = \frac{1}{(\tau_1 s+1)(\tau_2 s+1)(\tau_3 s+1)} \tag{28}$$

first applying the backward Taylor expansion:

$$H_{3\text{rd}}(s) \simeq e^{-\tau_1 s}e^{-\tau_2 s}e^{-\tau_3 s} = e^{-(\tau_1+\tau_2+\tau_3)s} \tag{29}$$

then the forward Taylor expansion:

$$H_{3\text{rd}}(s) \simeq e^{-(\tau_1+\tau_2+\tau_3)s} \simeq \frac{1}{1+(\tau_1+\tau_2+\tau_3)s} = \frac{1}{1+\tau_{\text{tot}}s} = H_{1\text{st}}(s) \tag{30}$$

we have derived an approximation of a third-order system to a first-order $H_{1\text{st}}(s)$ transfer function. This means that additionally to defining the gains of the RMs and ECs, the pole-based definition of the third-order system allows one to derive the mathematical approximation for the nearest first-order system, the dynamics of which are applicable in the ANDI controller for the virtual actuators.

Table 2 presents the selected poles for each component of the system, both for ANDI and INDI, along with the corresponding cascaded gains. It is notable that the poles of the EC are determined based on the error dynamics structure outlined in Sec. V. Hence, in INDI, the EC shares two poles with those in ANDI, whereas the latter includes an additional pole representing the actuator dynamics specific to that axis. These actuator dynamics are the slowest among the set of actuators used to control the axis, as the overall control is constrained by the slowest actuator. For the attitude EC, this corresponds to the quad motors' dynamics at 10.1 rad/s. For the position EC, it reflects the attitude dynamics at 1.57 rad/s, computed using Eq. (30) and the attitude RM poles.

In Fig. 10, the frequency responses of the attitude reference model from Eq. (22) and its first-order approximation from Eq. (30), utilizing the pole set defined in Table 2, are presented. It is evident that up to a frequency of 1 rad/s, the frequency responses of the two transfer functions are nearly identical. Therefore, one can infer that the first-order approximation can effectively approximate the third-order transfer function up to this frequency.

Similarly, in Fig. 11, the attitude INDI controller matches the frequency response of the ANDI controller up to 2 rad/s. Because

Table 2 ANDI RM and EC poles location and gains flight tuned for VSQP

System	Controller	$p1$	$p2$	$p3$	$k1$	$k2$	$k3$
Attitude RM	ANDI and INDI	4.71	4.71	4.71	1.57	4.71	14.14
Attitude EC	ANDI	4.50	4.50	10.1	1.84	5.82	19.10
Attitude EC	INDI	4.50	4.50	— —	2.25	9.00	— —
Position RM	ANDI and INDI	0.93	0.93	0.93	0.31	0.93	2.79
Position EC	ANDI	1.00	1.00	1.57	0.38	1.16	3.57
Position EC	INDI	1.00	1.00	— —	0.50	2.00	— —

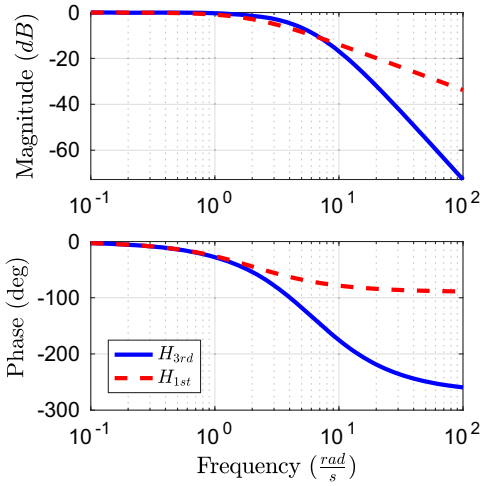

Fig. 10 Frequency response of the attitude dynamics transfer functions in Eqs. (22) and (30) with the poles defined in Table 2.

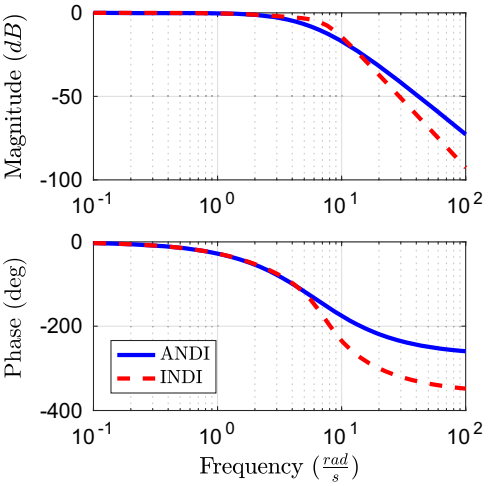

Fig. 11 Frequency response of $\eta(s)/\eta_{\text{des}}(s)$ in ANDI and INDI with the poles defined in Table 2.

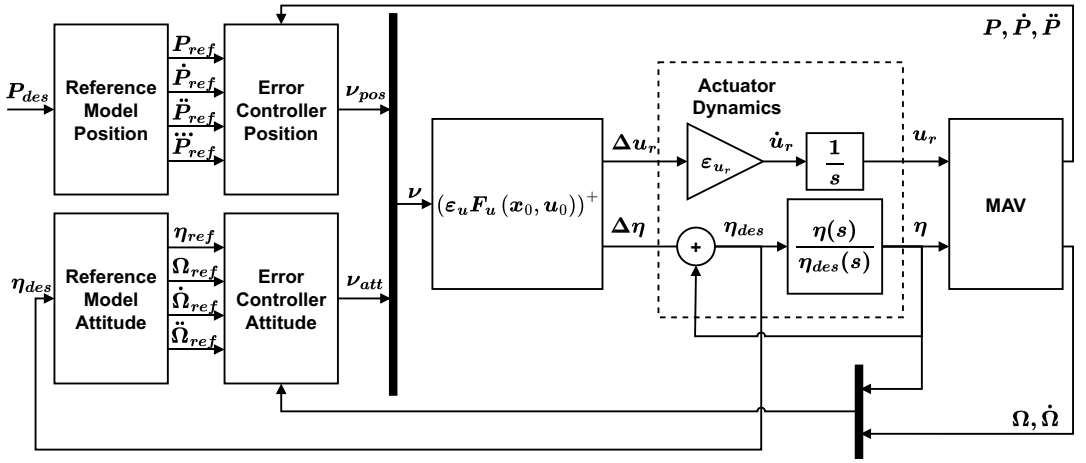

Fig. 12 Diagram of the unified ANDI controller with third-order attitude dynamics explicitly reported outside of the MAV block for analytical purposes.

we have shown that for ANDI, the transfer function $\boldsymbol{\eta}(s)/\boldsymbol{\eta}_{\text{des}}(s)$ simplifies to the RM dynamics $\boldsymbol{\eta}_{\text{ref}}(s)/\boldsymbol{\eta}_{\text{des}}(s)$ due to the unitary nature of the EC dynamics $\boldsymbol{\eta}(s)/\boldsymbol{\eta}_{\text{ref}}(s)$, the same conclusion can be drawn for INDI up to 2 rad/s. Figure 12 shows the adjusted ANDI unified controller with the identified attitude dynamics.

To ensure that the attitude angles are not commanded reference signals falling within the frequency range where the approximation is invalid, one can design a position reference model as depicted in Eq. (23), with poles specified as reported in Table 2. The Bode plot in Fig. 13 demonstrates that such a system already attenuates the magnitude by −10 dB at 1 rad/s, and further attenuates at higher frequencies.

As for the position EC, it is essential to acknowledge that the controller assumes first-order attitude dynamics, whereas they are actually third order. As a result, even in ANDI, when considering the SISO signal path allocating to the attitude angles, which have the slowest dynamics and thus dictate the dynamics of the entire system, the transfer function $\boldsymbol{P}(s)/\boldsymbol{P}_{\text{ref}}(s)_{\text{ANDI}}$ will not simplify to a unity gain. However, we can evaluate the impact of assuming the approximated first-order dynamics in the controller by substituting the simulation of the attitude dynamics $\boldsymbol{\eta}(s)/\boldsymbol{\eta}_{\text{des}}(s)_{\text{ANDI}}$ with the dynamics of the attitude reference model $\boldsymbol{\eta}_{\text{ref}}(s)/\boldsymbol{\eta}_{\text{des}}(s)$ and block reducing. Similarly, in INDI, $\boldsymbol{P}(s)/\boldsymbol{P}_{\text{ref}}(s)_{\text{INDI}}$ can be estimated by substituting $\boldsymbol{\eta}(s)/\boldsymbol{\eta}_{\text{des}}(s)_{\text{INDI}}$ with the product of $\boldsymbol{\eta}_{\text{ref}}(s)/\boldsymbol{\eta}_{\text{des}}(s)$ and $\boldsymbol{\eta}(s)/\boldsymbol{\eta}_{\text{ref}}(s)_{\text{INDI}}$ [as reported in Eq. (25)], and block reducing.

Figure 14 illustrates the frequency response of the transfer function $\boldsymbol{P}(s)/\boldsymbol{P}_{\text{ref}}(s)$ for both ANDI and INDI for the poles and gains of Table 2. It is noteworthy that the INDI transfer function displays positive magnitude amplification, starting from 0.4 rad/s

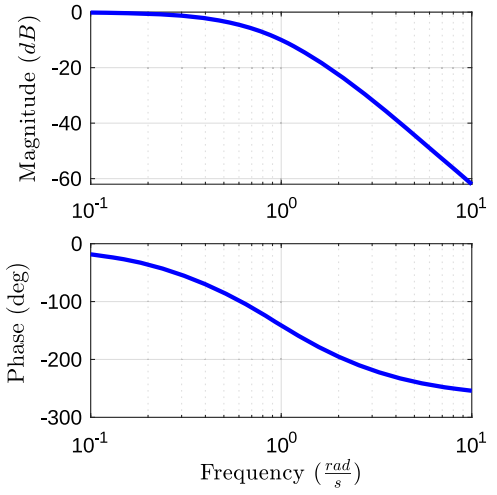

Fig. 13 Frequency response of $P_{\text{ref}}(s)/P_{\text{des}}(s)$ with the poles defined in Table 2.

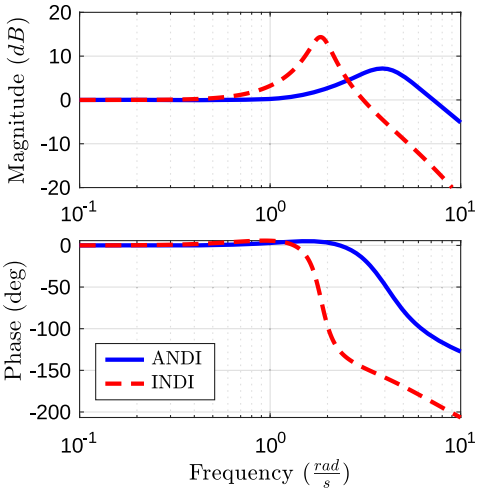

Fig. 14 Frequency response of $P(s)/P_{\text{ref}}(s)$ in ANDI and INDI with the poles defined in Table 2.

and reaching a peak of 13.9 dB at 1.9 rad/s. The phase remains approximately 0 deg until it starts to decline at 1.5 rad/s.

The ANDI transfer function instead shows positive magnitude amplification starting at a later frequency, 1.0 rad/s, coinciding with the onset of imprecisions due to the approximation of higher-order dynamics to first-order dynamics, and peaking at 7.0 dB at 4.0 rad/s. The phase remains approximately 0 deg until it starts to decline at 2.5 rad/s. It can be concluded that the ANDI controller exhibits comparatively favorable characteristics compared to the INDI controller: 1) smaller magnitude peak and 2) reduced phase lag occurring only at a 3) higher frequency.

Considering a set of reference signals describing a sinusoidal wave at a frequency of 0.8 rad/s, one can conclude from Fig. 14 that whereas an ANDI controller would be capable of precisely tracking the input signal (magnitude of 0.05 dB and phase of 1.69 deg), the INDI controller would consistently slightly lead and overshoot the reference signal (magnitude of 2.00 dB and phase of 5.51 deg).

VIII. Test 1: Position Sinusoidal Tracking

This observation is further confirmed by conducting a simple simulation in Simulink, where the drone attempts to track an input sinusoidal signal in the longitudinal body direction. The simulation involves two actuators, namely thrust and pitch angle, and is constructed based on the structure depicted in Fig. 15. The absence of a pusher in the test setup serves the purpose of ensuring that the pitch angle must be actively utilized throughout to achieve positioning. This restriction effectively confines the system dynamics to the pitch dynamics, aligning with the considerations of the SISO transfer

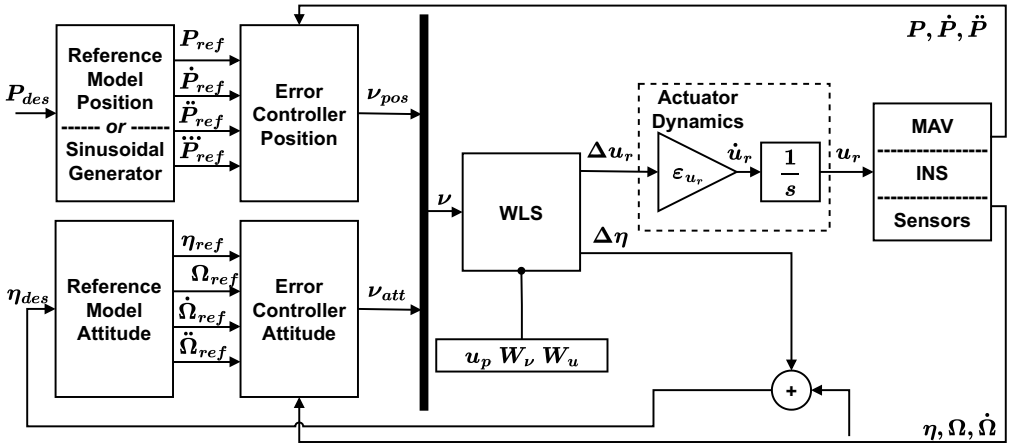

Fig. 15 Diagram of the unified ANDI controller as implemented on the VSQP.

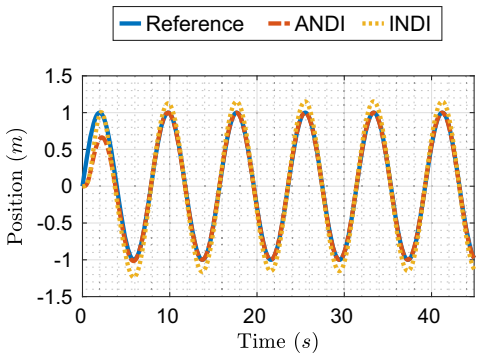

Fig. 16 Simulation longitudinal position sinusoidal tracking at 0.8 rad/s.

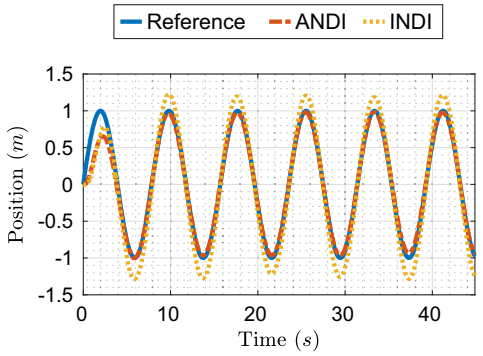

Fig. 17 Flight test longitudinal position sinusoidal tracking at 0.8 rad/s.

functions discussed in Sec. VII. It is worth noting that one deviation from Fig. 12 is that the position reference signals are generated analytically rather than using RMs. This step is taken to calculate the perfect reference signals to track the position sinusoidal and to isolate the response to only the error-controller dynamics, ensuring that the position reference model does not interfere. The simulation files and all presented test data can be found at [20].

In Fig. 16, the results of the position sinusoidal tracking test are depicted. As anticipated, the ANDI controller tracks the reference signal nearly perfectly, whereas the INDI controller consistently overshoots the reference signals by approximately 0.25 m. This test was validated in real life through an indoor test with the VSQP, utilizing an infrared tracking positioning system. The tracking of the position sinusoidal during the flight test can be found in Fig. 17.[¶] Remarkably, the flight test results closely align with the simulation results, with the INDI controller demonstrated to perform worse than the ANDI controller.

Slight differences between the simulation and flight test exist, particularly concerning the magnitude and periodicity of the position error, as illustrated in Figs. 18 and 19. These discrepancies are believed to arise from intrinsic modeling inaccuracies of real-life systems, as well as the fact that the simulation is conducted purely in two dimensions, whereas in real life, the drone is executing control allocation to accommodate positioning in three-dimensional space along with the three attitude angles.

IX. Test 2: Overactuation Test

In Fig. 12, control allocation is performed through the pseudoinversion of the effectiveness matrix. However, this is just one of many

[¶]A video of the presented flight tests can be found at https://www.youtube.com/watch?v=yLcbNwS9VxM&ab_channel=MAVLabTUDelft.

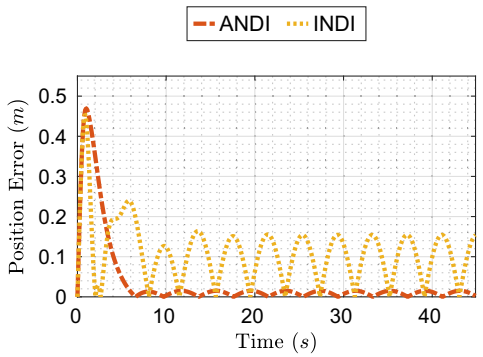

Fig. 18 Simulation longitudinal position error.

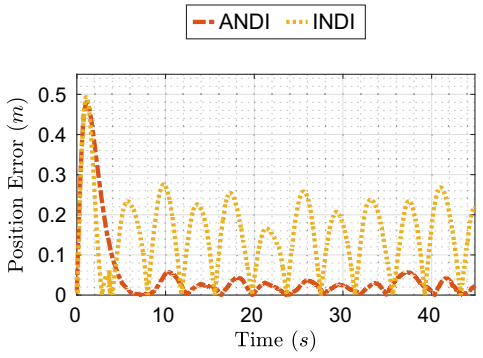

Fig. 19 Flight test position error.

methods available for solving the control allocation. In truth, as shown in Fig. 15, the control allocation executed onboard VSQP utilizes a WLS [1,3] routine, with specific adaptations to incorporate the use of pusher motors and the lift generated by the wing [21]. The advantage of WLS lies in its ability to incorporate saturation limits, a hierarchy between the pseudocontrol vectors and a preferred state for the actuators in the control allocation process.

It is important to note that the VSQP is partially overactuated along its body x axis, which means it can hover steadily with a positive pitch angle at a specific point in space by compensating with the pusher motor. Such capability can be particularly advantageous during transitions to forward flight and hover. In Ref. [2], transitions are performed by introducing a desired pitch along with changing airspeed. This approach helps to steer the drone away from states where aerodynamic effects, difficult to model precisely, disturb its stability. For instance, when the wing is retracted and the drone is moving forward with a positive pitch, the exposed section of the wing at the front creates a pitch moment that could potentially saturate the rear motor. To mitigate this scenario, setting a slightly negative preferred pitch angle has been found to be effective. Another reason for specifying a desired pitch angle is that VSQP was designed to land on moving ships. Therefore, being able to partially mimic the deck pose during landing can be beneficial for achieving precise and robust landings.

It is evident how maintaining precise trajectory tracking and being able to match a desired pitch angle are crucial aspects of the control of VSQP. Therefore, a second test is devised to demonstrate the advantages of the ANDI controller over the INDI controller. In this test, a sinusoidal signal with a frequency of 0.8 rad/s is supplied to the control allocation as the preferred pitch angle. This frequency is selected again because, as shown in Fig. 11, both controllers should be capable of perfectly and identically following the attitude reference signal. However, it is anticipated that in INDI, due to the omission of the slow dynamics of the attitude angles, the thrust and pusher motor command will not be optimally calculated to maintain precise position tracking simultaneously.

Figure 20 illustrates the pitch-related signals during the overactuation test for both the ANDI and INDI controllers. The preferred signal is a sine wave with a frequency of 0.8 rad/s. To ensure that the control allocation prioritizes matching the preferred pitch angle wave, only the pitch angle is assigned a cost in the secondary objective of the WLS routine. The output of the control allocation is then the preferred pitch signal itself, which is fed to the attitude RM as depicted in Fig. 12, and the associated thrust and pusher motor commands to maintain the hover position. Because both controllers receive the same attitude desired and utilize the same attitude RM, their attitude outputs are identical.

As expected, Fig. 20 confirms that both the ANDI and INDI controllers are proficient in accurately tracking the pitch reference signal. However, Fig. 21 reveals that while accomplishing this task, the INDI controller maintains an average position error of 0.42 m, whereas the ANDI controller exhibits a much lower average position error of 0.17 m, indicating its superior precision.

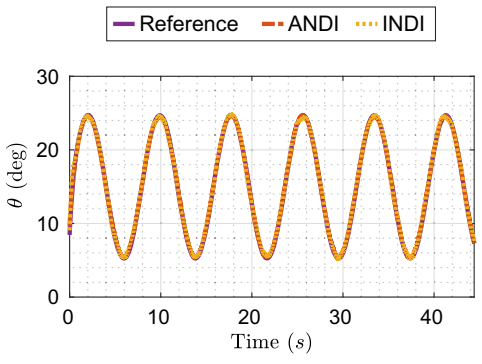

Fig. 20 Overactuation test pitch sinusoidal tracking at 0.8 rad/s.

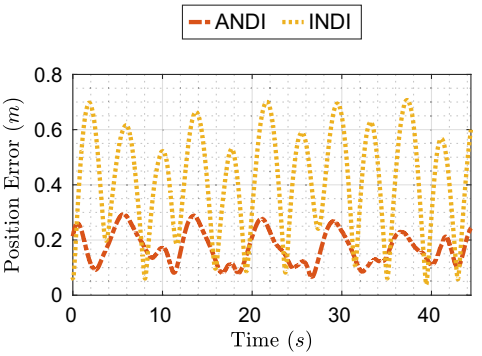

Fig. 21 Overactuation test position error.

X. Conclusions

The aim of this Technical Note was to demonstrate how a Unified actuator nonlinear dynamic inversion (ANDI) controller with pole-based reference model and error controller is a suitable solution for precisely tracking trajectories of a platform that integrates both fast and slow actuators, as seen in the variable skew quad plane. Four main conclusions can be drawn from the test flight results and theoretical considerations presented in this Note:

1) The ANDI control law is demonstrated for the first time to function effectively on a real platform in a real-life environment.

2) A novel method to extend the ANDI control law for performing guidance tasks within a unified-controller structure is successfully presented and validated.

3) ANDI is shown to outperform INDI on platforms with varying and slow actuator dynamics in tracking position trajectories.

4) ANDI demonstrates superior performance over INDI in efficiently utilizing overactuated axes while maintaining precise positioning.

Acknowledgments

Founded with the support of the Royal Dutch Navy and the Royal Coast Guard, this initiative aims to foster collaboration and innovation in maritime endeavors.

References

[1] De Ponti, T. M. L., Smeur, E. J. J., and Remes, B. W. D., "Incremental Nonlinear Dynamic Inversion Controller for a Variable Skew Quad Plane," *2023 International Conference on Unmanned Aircraft Systems (ICUAS)*, IEEE Publ., Piscataway, NJ, 2023, pp. 241–248. https://doi.org/10.1109/ICUAS57906.2023.10156289

[2] van Wijngaarden, D. C., and Remes, B. D. W., "INDI Control for the Oblique Wing-Quad Plane Drone," *International Micro Air Vehicle Conference and Flight Competition*, TU Delft, 2022, https://www.imavs.org/papers/2022/14.pdf.

[3] Smeur, E. J. J., Hoppener, D. C., and Wagter, C. D., "Prioritized Control Allocation for Quadrotors Subject to Saturation," *International Micro Air Vehicle Conference and Flight Competition*, 2017, https://www.imavs.org/papers/2017/6.pdf.

[4] Blaha, T. M., Smeur, E. J. J., and Remes, B. D. W., "A Survey of Optimal Control Allocation for Aerial Vehicle Control," *Actuators MDPI*, Vol. 12, No. 7, 2023, Paper 282. https://doi.org/10.3390/act12070282

[5] Smeur, E. J. J., de Croon, G. C. H. E., and Chu, Q., "Cascaded Incremental Nonlinear Dynamic Inversion for MAV Disturbance Rejection," *Control Engineering Practice*, Vol. 73, 2018, pp. 79–90. https://doi.org/10.1016/j.conengprac.2018.01.003

[6] Smeur, E. J., De Croon, G. C., and Chu, Q., "Gust Disturbance Alleviation with Incremental Nonlinear Dynamic Inversion," *IEEE/RSJ International Conference on Intelligent Robots and Systems*, Inst. of Electrical and Electronics Engineer, New York, 2016, pp. 5626–5631. https://doi.org/10.1109/IROS.2016.7759827

[7] Pfeifle, O., and Fichter, W., "Cascaded Incremental Nonlinear Dynamic Inversion for Three-Dimensional Spline-Tracking with Wind Compensation," *Journal of Guidance, Control, and Dynamics*, Vol. 44, No. 8, 2021, pp. 1559–1571. https://doi.org/10.2514/1.G005785

[8] Smeur, E. J. J., Chu, Q., and de Croon, G. C. H. E., "Adaptive Incremental Nonlinear Dynamic Inversion for Attitude Control of Micro Air Vehicles," *Journal of Guidance, Control, and Dynamics*, Vol. 39, No. 3, 2016, pp. 450–461. https://doi.org/10.2514/1.G001490

[9] Bhardwaj, P., Raab, S. A., Zhang, J., and Holzapfel, F., "Integrated Reference Model for a Tilt-Rotor Vertical Take-Off and Landing Transition UAV," *2018 Applied Aerodynamics Conference*, AIAA Paper 2018-3479, 2018. https://doi.org/10.2514/6.2018-3479

[10] Raab, S. A., Zhang, J., Bhardwaj, P., and Holzapfel, F., "Proposal of a Unified Control Strategy for Vertical Take-Off and Landing Transition Aircraft Configurations," *2018 Applied Aerodynamics Conference*, AIAA Paper 2018-3478, 2018. https://doi.org/10.2514/6.2018-3478

[11] Mancinelli, A., Remes, B. D. W., de Croon, G. C. H. E., and Smeur, E. J. J., "Unified Incremental Nonlinear Controller for the Transition Control of a Hybrid Dual-Axis Tilting Rotor Quad-Plane," *IEEE Transactions on Robotics*, Vol. 41, 2025, pp. 306–325. https://doi.org/10.1109/TRO.2024.3498372

[12] Sieberling, S., Chu, Q. P., and Mulder, J. A., "Robust Flight Control Using Incremental Nonlinear Dynamic Inversion and Angular Acceleration Prediction," *Journal of Guidance, Control, and Dynamics*, Vol. 33, No. 6, 2010, pp. 1732–1742. https://doi.org/10.2514/1.49978

[13] Wang, X., Van Kampen, E., Chu, Q. P., and De Breuker, R., "Flexible Aircraft Gust Load Alleviation with Incremental Nonlinear Dynamic Inversion," *Journal of Guidance, Control, and Dynamics*, Vol. 42, No. 7, 2019, pp. 1519–1536. https://doi.org/10.2514/1.G003980

[14] Zhou, Y., Ho, H. W., and Chu, Q., "Extended Incremental Nonlinear Dynamic Inversion for Optical Flow Control of Micro Air Vehicles," *Aerospace Science and Technology*, Vol. 116, 2021, Paper 106889. https://doi.org/10.1016/j.ast.2021.106889

[15] Johnson, E., and Kannan, S., "Adaptive Flight Control for an Autonomous Unmanned Helicopter," *AIAA Guidance, Navigation, and Control Conference and Exhibit*, AIAA Paper 2002-4439, 2002. https://doi.org/10.2514/6.2002-4439

[16] Raab, S. A., Zhang, J., Bhardwaj, P., and Holzapfel, F., "Consideration of Control Effector Dynamics and Saturations in an Extended INDI Approach," *AIAA Aviation 2019 Forum*, AIAA Paper 2019-3267, 2019. https://doi.org/10.2514/6.2019-3267

[17] Bhardwaj, P., Raab, S. A., and Holzapfel, F., "Higher Order Reference Model for Continuous Dynamic Inversion Control," *AIAA Scitech 2021 Forum*, AIAA Paper 2021-1130, 2021. https://doi.org/10.2514/6.2021-1130

[18] Steffensen, R., Steinert, A., and Smeur, E. J. J., "Nonlinear Dynamic Inversion with Actuator Dynamics: An Incremental Control Perspective," *Journal of Guidance, Control, and Dynamics*, Vol. 46, No. 4, 2023, pp. 709–717. https://doi.org/10.2514/1.G007079

[19] Andrews, W. H., Sim, A. G., Monaghan, R. C., Felt, L. R., McMurtry, T. C., and Smith, R. C., "AD-1 Oblique Wing Aircraft Program," *SAE Transactions*, Vol. 89, 1980, pp. 3571–3577. https://doi.org/10.4271/801180

[20] De Ponti, T. M. L., "Dataset of the Paper Unified Actuator Nonlinear Dynamic Inversion Controller for the Variable Skew Quad Plane," 4TU.ResearchData. Dataset, 2024. https://doi.org/10.4121/8dc704cb-80b0-493d-9723-5ec25f2667c9.

[21] Karssies, H., and De Wagter, C., "Extended Incremental Non-Linear Control Allocation (XINCA) for Quadplanes," *International Journal of Micro Air Vehicles*, Vol. 14, 2022, Paper 17568293211070825. https://doi.org/10.1177/17568293211070825

K. Wise
Associate Editor